



Smart helical swimmer: Nested and uncoiled designs

Z.Y. Zhang^a, Y.B. Song^b, Y.F. Wang^c, C.G. Wang^{a,*}

^a National Key Laboratory of Science and Technology for National Defence on Advanced Composites in Special Environments, Harbin Institute of Technology, Harbin 150001, PR China

^b State Key Laboratory of Urban Water Resource & Environment, School of Chemistry and Chemical Engineering, Harbin Institute of Technology, Harbin 150001, PR China

^c Department of Aeronautics and Astronautics, Fudan University, Shanghai 200433, PR China



ARTICLE INFO

Keywords:
Nested helical structure
Uncoiled structure
Shape memory polymer
Smart material
Propulsive motility

ABSTRACT

Micro- and nanobots capable of controlled propulsion at low Reynolds number are expected to change many aspects of medicine by enabling targeted diagnosis and therapy and allowing minimally invasive surgery. Several types of helical swimmers with different actuation mechanisms have been proposed. As materials become smarter and more advanced, the boundaries between robots and materials have become less apparent. The goal of the present work is to develop a smart nested design or uncoiled design of temperature-sensitive helical swimmers adapted to low Reynolds number. The regulation of swimming velocity should provide numerous options for designing various small-sized, high-speed, motion-controllable robots for environmental and biomedical applications. To investigate the thermomechanical properties of swimmers, we present systematically theoretical modeling, experiments, and numerical calculations of temperature-sensitive shape-memory helical structures. Moreover, this work demonstrates differences in movement attributed to single or nested, folded or unfolded, and coiled or uncoiled helical structures with diverse configurations, which provide a reliable design strategy. The swimming capability can be regulated by the configurations, especially the swimmer radius. We also provide an intuitive Ashby selection map and explain the mechanical mechanism by which structure affects locomotion capability. The proposed smart helix-based swimmers should find thermomechanical coupling in applications involving active matter, biomedical sensing, and targeted drug delivery.

1. Introduction

Nature inspires the development of smart micro- and nanobots, of which the helix is one of the most common structural motifs. Helices appear in different dimensions and are required in numerous practical applications (see Fig. 1) [1–3]. Inspired by the “run-and-tumble” behavior of *Escherichia coli* (*E. coli*), microswimmers driven by rotation of the spiral tail have been designed and applied to diverse biomedical applications, including targeted drug delivery [4–6], precision nano-surgery [7,8], and diagnostic sensing [9,10]. These bots represent a class of micromachines that can convert external chemical [11,12], acoustic [13,14], optical [15–17], or electromagnetic [18–20] energy into the kinetic energy generated by the swimming. The geometry and configuration of these helical swimmers significantly affects their motion performance [21–25]. The natural world inspires unconventional locomotion and navigation principles that in turn can be implemented by using smart materials. Critically, shape-memory polymers (SMPs) are

morphologically responsive materials with a substantial potential for a variety of applications in both engineering industries (e.g., aeronautics, electronics) and biomedical industries (e.g., as stents or scaffolds for the delivery of therapeutics and cells) [26–31]. Therefore, the mechanical and functional capabilities of SMP-based helical microrobots are attractive because they create enticing opportunities in biomedicine, sensing, and smart healthcare [32–37].

The fundamental principles and motion control of helical swimming machines, with rich underlying physics and chemistry, have been used in several comprehensive articles [38–43]. A wide range of physical parameters has been tested to improve the classic resistive force theory in experiments on macroscopic swimmers in highly viscous fluids [22, 44], and the complementary numerical simulations are conducted to readily compute force, torque, and drag [44] as well as the corresponding parametric analysis [45] for micro- or nanobots driven by a rotating helical tail. In particular, some simple and versatile methods [19,20] have been presented to establish a reconfigurable helical body

* Corresponding author.

E-mail address: wangcg@hit.edu.cn (C.G. Wang).

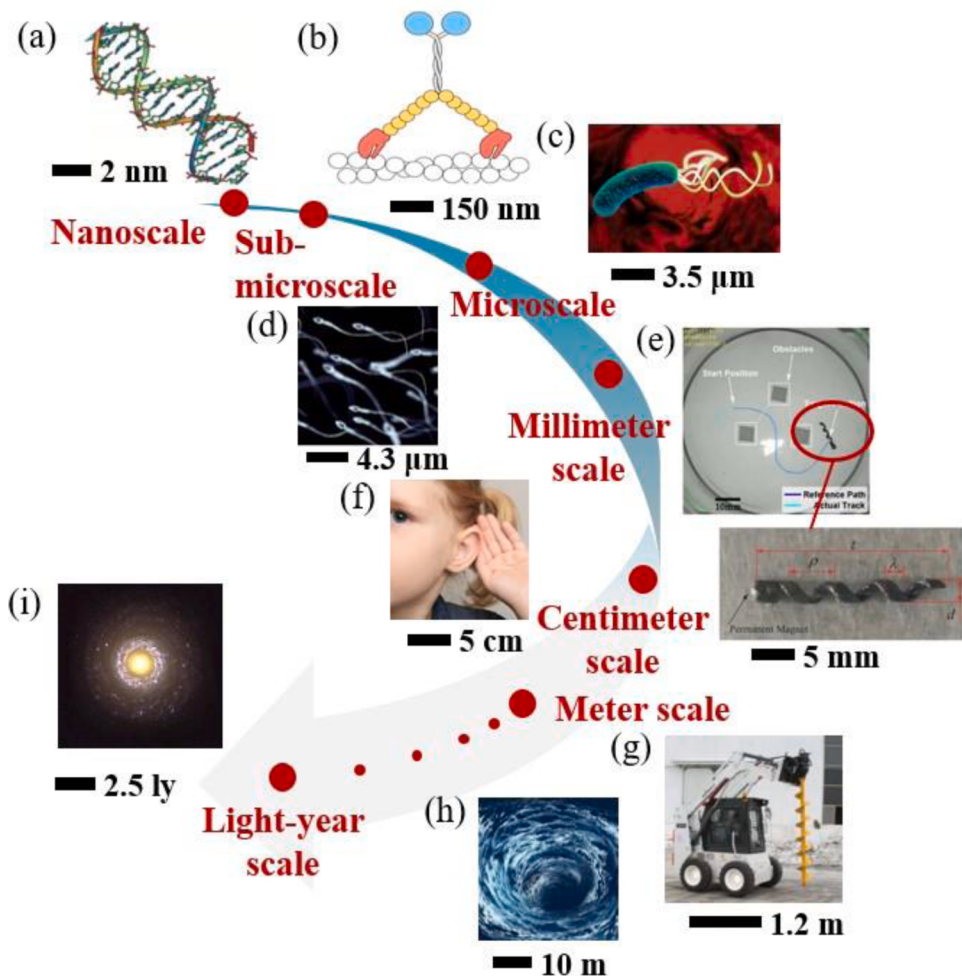


Fig. 1. Schematic representation of natural and bioinspired helical structures on different scales. (a) The double helix structure of DNA. (b) Myosin is made up of one or two heavy chains and several light chains [1]. (c) *H. Pylori* is composed of multiple helical tails. (d) The swimming mode of the human sperm consists of rotating with the “head” as a center, and the spiral movement cleverly offsets the unilateral swing to achieve symmetry. (e) Miniature magnetic helical swimmer and its obstacle-avoidance ability [2,3]. (f) The human cochlea grows in a spiral line. (g) Auger drilling machine for clearing snow. (h) Spiral vortex in the sea. (i) A Hubble Space Telescope (HST) image of spiral galaxy NGC 7742 (Credit: NASA/ESA/STSCI/AURA).

that can continuously morph in accordance with the properties of the surrounding fluid. Such a feature can allow the swimmer to pass through constrictions and enhance its locomotion. The swimming characteristics, dynamic morphologies, and velocity-independent planar path following strategy [43,46] of miniature rotating magnetic swimmers with soft tails have been studied systematically. Inspired by multi-flagellate bacteria such as *E. Coli* Fig. 1(c), biomimetic-propulsion helical propellers with multiple tails have been proposed [47,48]. The hierarchical helical microswimmer [49] significantly improves propulsive motility while maintaining stability and resilience at a decent level. Moreover, the magnetically induced shape-memory effect of the polyetherurethane sample is demonstrated [50], and a change process in shape from a corkscrew-like spiral (temporary shape) to a plane stripe (permanent shape) is shown to occur within 22 s [51]. Another class of microrobots, stimuli-responsive soft materials [52,53] such as poly(*N*-isopropylacrylamide), can serve as controlled actuators by using external control signals to trigger a specific material response, thereby providing microrobots with advanced functionalities and locomotion strategies.

Numerous publications discuss the theory and relevant experiments to analyze the mechanical and kinematic properties of helical structures [54]. However, in most previous research, external power is required for the helical swimmer to move. This power may come from, e.g., the local chemical energy (e.g., the catalytic decomposition of hydrogen peroxide, which generates hydrogen bubbles for self-propulsion) [11,12,55]. Some biomimetic strategies [56–58] work well on the microscale by using physics principles. However, these methods depend heavily on the mechatronic components. Thus, no controllable external pulling source

is available on the microscale. But applying forces and torques by the gradient magnetic fields is an available and practicable means to drive untethered microrobots [59–61]. In addition, the common way to optimize the swimming performance from the own structure design is relatively simple, such as varying the wavelengths, radii, lengths of the tail, and the presence or absence of a head [44,62–64]. Moreover, existing swimming robots with the thermally or magnetically induced shape memory effect [65,66] cannot flexibly morph and reshape (i.e., transfer between two simple configurations: temporary shape and permanent shape). Furthermore, although the thermomechanical properties of the SMP have been well developed in both theory and experiment [67–70], rare are the numerical analyses for the SMP with special configurations, such as the helix.

In this study, we focus on the structural design of a type of smart microswimmer that regulates its velocity and motility to adapt to various complex and ever-changing environments. The article is organized as follows: Section 2 introduces the thermomechanical constitutive model and helical propulsion model. Section 3 discusses the technical details of SMP preparation and the platform. Section 4 further presents the numerical calculations of the nested helical structures and uncoiled structures, as well as comparisons between simulations, theory, and experiments. Finally, Section 5 states the main conclusions of this work.

2. Locomotion of smart helical swimmers

In view of describing the thermomechanical mechanism of SMP and swimming behaviors along the axis of the helical robot with a rigidly

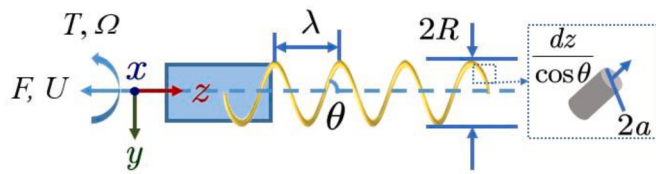


Fig. 2. Definition of parameters for a helical swimmer with a rigidly attached cylindrical head. The force F and torque T represent the sum of all non-fluidic loads.

attached head, a modified linear constitutive model [68] and a symmetric propulsion matrix [21] relating only three constants are proposed in this section, respectively.

The modified linear constitutive model expresses the fact that in the process of creep recovery under no-load which follows loading with creep strain ε_c , a certain part of ε_c remains as irrecoverable strain. The thermal expansion is considered to be independent in this model. The model provides the basis for our understanding of the smart material in this work. On the other hand, the motion of the helical structure, can be considered in only two degrees of freedom and described by only three constants, which depend on the fluid viscosity and geometrical parameters.

2.1. Thermomechanical constitutive model

To describe the deformation mechanism of SMPs, we introduce the standard linear viscoelastic model. Considering the thermal expansion and assuming that the expansion is independent of mechanical behavior, the stress-strain-temperature relationship can be expressed as

$$\dot{\varepsilon} = \frac{\dot{\sigma}}{E} + \frac{\sigma}{\mu} - \frac{\varepsilon - \varepsilon_s}{\Delta} + \alpha \dot{T}, \quad (1)$$

where ε and σ are the strain and stress, respectively (the dot indicates the time derivative), E , μ , and Δ are the elastic modulus, viscosity, and retardation time, respectively, and α and T are the temperature and coefficient of thermal expansion, respectively. The creep irrecoverable strain ε_s is given by $\varepsilon_s = C(\varepsilon_c - \varepsilon_l)$, where ε_c is the critical strain, and ε_l and C depend on temperature.

With SMPs, E , μ , Δ , C , and ε_l depend on temperature. These variables expressed on a logarithmic scale increase linearly in T_g/T in the glass-transition region $T_g - T_w \leq T \leq T_g + T_w$, where T_g is the glass-transition temperature, and T_w is a certain temperature. In this paper, we use $T_w = 15^\circ\text{C}$. These material parameters can be expressed as follows [68,69]:

$$X = X_g \exp \left[a_x \left(\frac{T_g}{T} - 1 \right) \right], \quad (2)$$

where X represents one of the variables E , μ , Δ , or C . X_g is the value at $T = T_g$, and a_x is the slope of each straight line on a semi-log plot. Similarly,

$$\varepsilon = \varepsilon_g \exp \left[- a_\varepsilon \left(\frac{T_g}{T} - 1 \right) \right]. \quad (3)$$

2.2. Helical propulsion model

A detailed propulsion matrix for a helical structure without a head is available in our previous work [49]. Consider a rigidly attached head: the motion of the symmetrical helical swimmer (as shown in Fig. 2) with the total external force F and torque T can be described only by several constants, which are expressed in matrix form as follows [21]:

$$\begin{bmatrix} F \\ T \end{bmatrix} = \begin{bmatrix} A + \Pi_U & B \\ B^T & C + \Pi_\Omega \end{bmatrix} \cdot \begin{bmatrix} U \\ \Omega \end{bmatrix}, \quad (4)$$

where U is the linear velocity along the body axis, Ω is the rotating angular velocity, Π_U and Π_Ω are respectively the translational and rotational drag coefficients for the head. The coefficients are identical for helical swimmers with the same heads. The coefficients A , B , and C in the matrix depend on the fluid viscosity and on the geometrical parameters of the helical swimmer, which can be estimated as follows: [21]

$$\begin{aligned} A &= (\eta_{II} \sin^2 \theta + \eta_{\perp} \cos^2 \theta) \frac{2\pi n R}{\cos \theta}, \\ B &= (\eta_{II} - \eta_{\perp}) 2\pi n R^2 \sin \theta, \\ C &= (\eta_{II} \cos^2 \theta + \eta_{\perp} \sin^2 \theta) \frac{2\pi n R^3}{\cos \theta}, \end{aligned} \quad (5)$$

where $\theta = \tan^{-1} \left(\frac{2\pi R}{\lambda} \right)$, λ is the pitch of the helix, n is the number of the turns of the helix, R is the radius of the helix, and η_{II} and η_{\perp} are the commonly used drag coefficients of Gray and Hancock [71] respectively, which are expressed as

$$\eta_{\perp} = \frac{2\pi \mu}{\ln \frac{2a}{a} - \frac{1}{2}}, \quad \eta_{II} = \frac{4\pi \mu}{\ln \frac{2a}{a} + \frac{1}{2}}, \quad (6)$$

where μ is the dynamic viscosity of the fluid, and a is the radius of the filament. These geometric parameters are described in Fig. 2.

Given that we consider uniform magnetic fields, the helical swimmers discussed herein are rotated by pure magnetic torques without magnetic force. Therefore, from Eq. (4), the relationship between the translation velocity U and the rotation speed Ω is:

$$U = - \frac{B}{A + \Pi_U} \Omega, \quad (7)$$

where $\Pi_U = 6\pi\mu R$ [59].

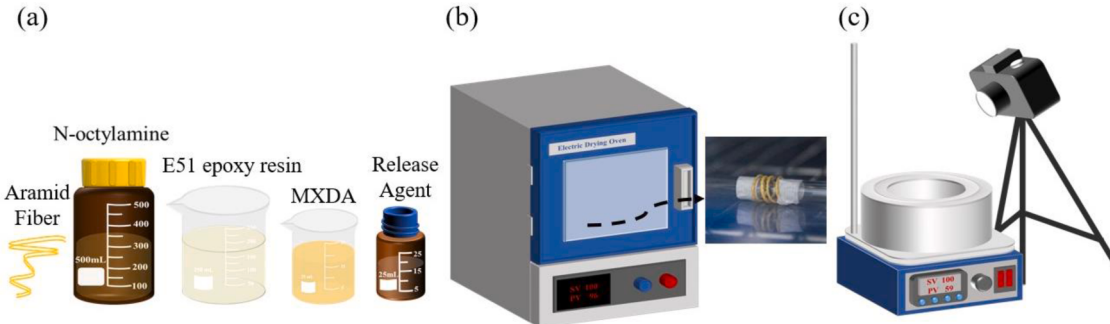


Fig. 3. Fabrication process of the SMP helical structure. (a) Preparation of the materials. From left to right: aramid filament, N-octylamine, E51 epoxy resin, MXDA, and release agent. (b) Displacement loading of the sample under 100°C in the electric drying oven. (c) Experimental apparatus: DF-101S Heat Collection-Constant Temperature Magnetic Stirrer and camera.

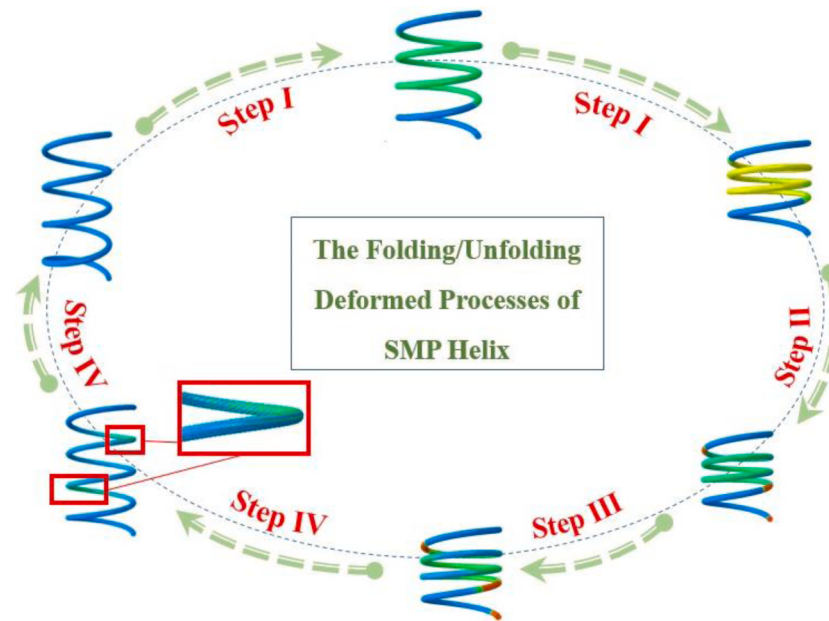


Fig. 4. Folding-unfolding deformed processes of SMP helix structure. (Step I) Folding stage under external load, (Step II) cooling stage, (Step III) unloading stage, (Step IV) heating recovery stage.

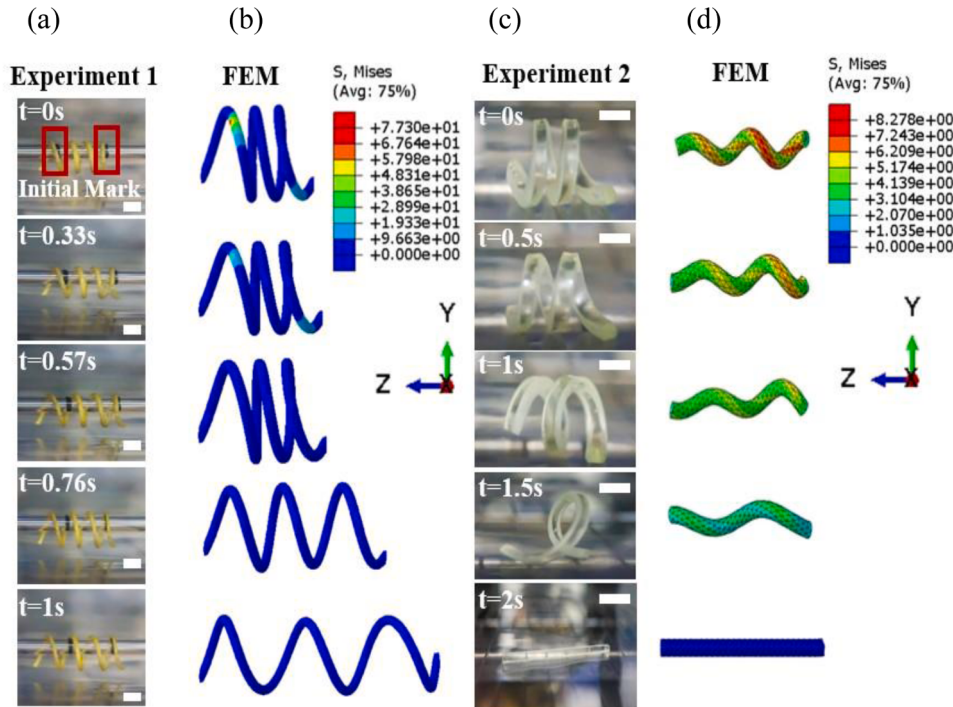


Fig. 5. Deployable process of SMP helix structure. (a, b) The unfolding process in experiment and simulation results of a SMP helix within 1 s, respectively. The scale bars are 3 mm. (c) The uncoiling process of the pure resin helix in the electric drying oven. The scale bars are 5 mm. (d) Results of numerical calculation of the uncoiling process.

According to the matrix (Eq. (4)), the linear and rotational speed contributions are additive in the low Reynolds number environment. Therefore, in the following simulation of the helical propulsion, the complex fluid environment can be simplified into two independent control regions, which simulate the longitudinal motion and rotation respectively.

3. Experimental platform

This section presents the experimental platform used to prepare SMP-based helical structures and evaluate their thermomechanical properties. The objective of our experiments is to prepare SMP-based materials with superior properties such as shape-recovery ratio and verify the realizability of the temperature-sensitive helical tail. Section 3.1 explains the preparation process of SMPs, and Section 3.2 presents

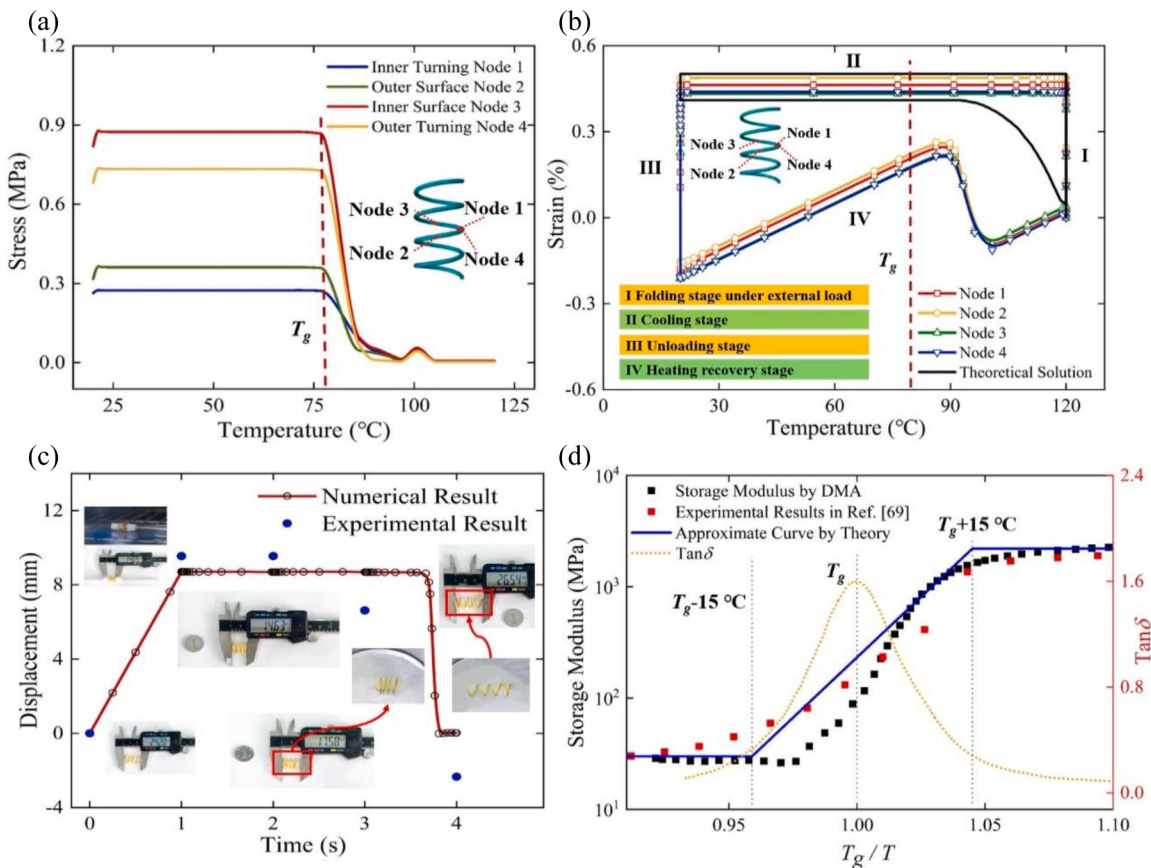


Fig. 6. Characterization of the mechanical properties of the SMP helix. (a) Relationship between stress and temperature of the representative nodes on the helix structure. (b) Relationship between strain and temperature in the four stages of the whole cycle. (c) Relationship between the displacement in the loading direction and time. Insets show the length of the helix in each step of the thermomechanical experiment. (d) Dynamic mechanical analysis of SMP. A comparison among our experimental results, results in Ref. [69], and approximate curve obtained by Eq. (2) is given.

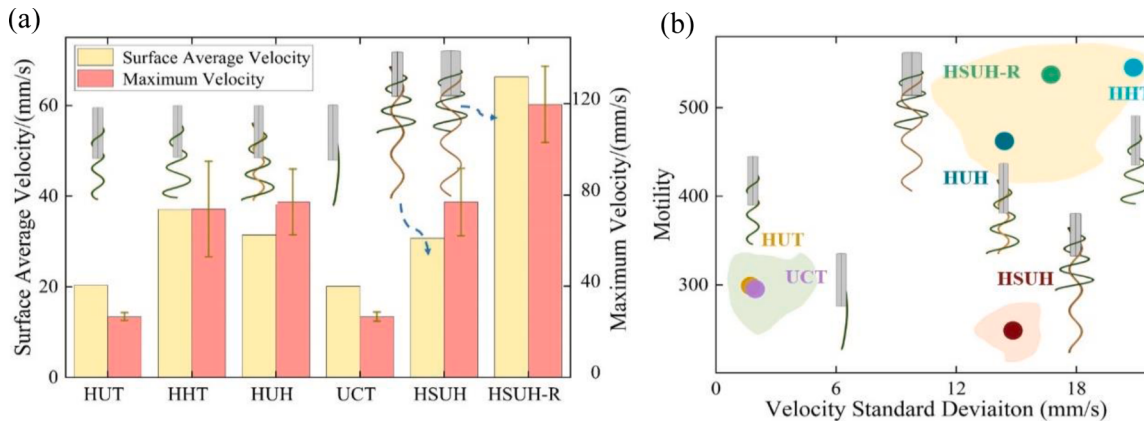


Fig. 7. Comparison of comprehensive athletic ability of the mode design with variable configurations. (a) Quantitative comparison of surface average velocity and maximum velocity for different prototypes. The swimmers are driven at 5 Hz. (b) Ashby selection map. The map shows the dimensionless motility of different structures against structural stability. All swimmers are rotated in the same viscosity flow field of 96.4 mPa s at 5 Hz.

the specific operational steps to realize the shape memory function of the helical tail.

3.1. Material preparation

To fabricate the SMP solution, N-octylamine and M-xylylene diamine (MXDA) are incorporated into E51 epoxy resin at a mass ratio (E51 epoxy resin/ N-octylamine/ MXDA) of 1 : 0.1646 : 0.0868 Fig. 3(a). After vacuuming the mixture several times to remove all bubbles, the

aramid filament is fully immersed into the solution. The filament must be lightly scratched to break the surface tension, making it easier for bubbles to escape. The SMP helix is shaped by winding at 100 °C for 3 h. To release the mold, the release agent is evenly spread on the surface of the glass mold in advance.

3.2. Experimental operation

The folding and unfolding process is done in four stages: (Step I)

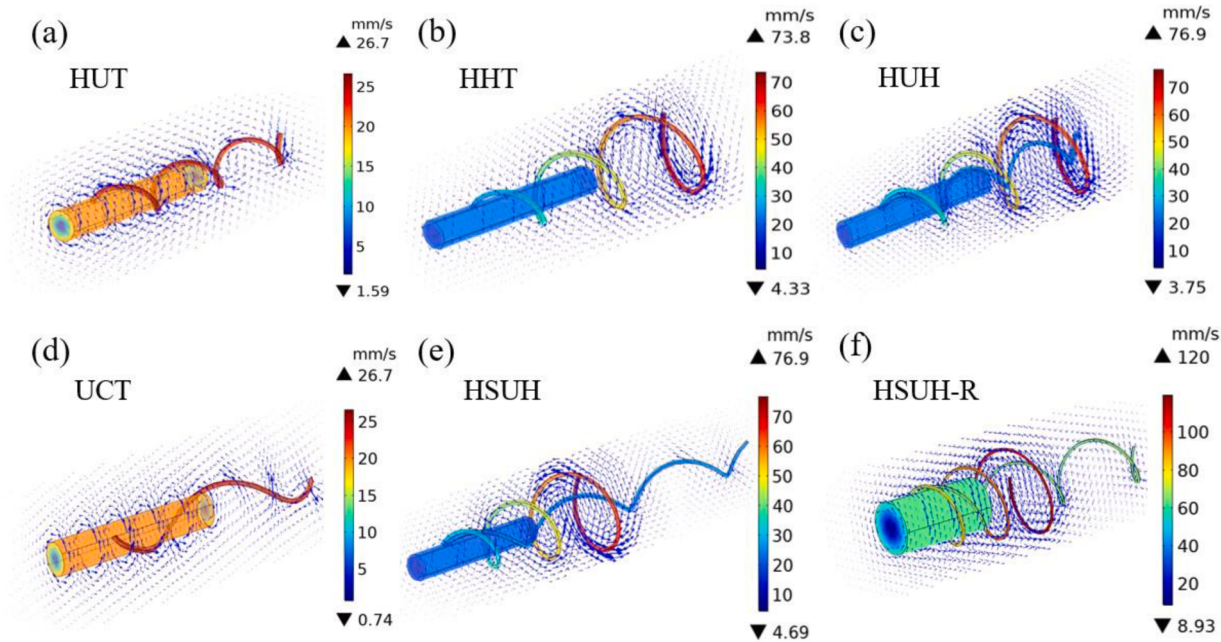


Fig. 8. The swimmers tend to move with the flow induced by the rotation of the tail. (a–f) present the surrounding velocity field of HUT, HHT, HUH, UCT, HSUH, HSUH-R structures, respectively. Velocity vectors (arrow volume) of the flow on cross section of the channel due to clockwise rotation of the swimmer about the z-axis, and the velocity field (shaded colors) on the swimmer.

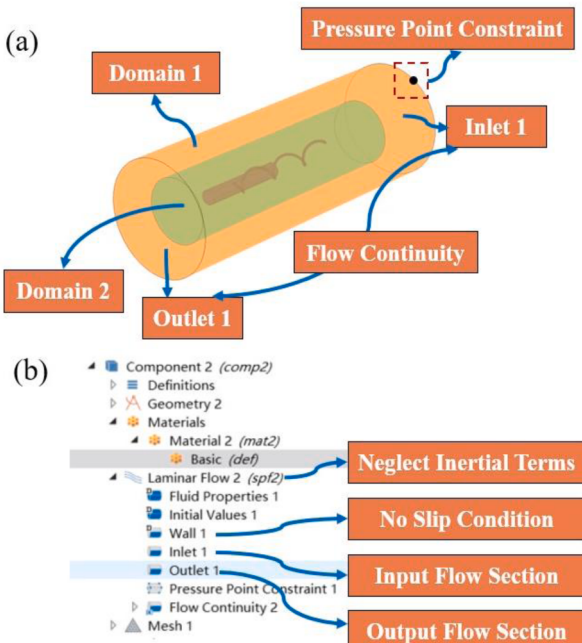


Fig. A1. . Modeling details in COMSOL Multiphysics®. (a) Model of helical swimming structure within a lumen flow environment. (b) Laminar flow dropdown menu.

Table A1

. Fluid parameters used in numerical modeling.

Property	Value	Units
Fluid Density	964	kg/m ³
Fluid Viscosity	0.0964	Pa s
Angular Velocity	31.416	rad/s
Linear Flow Rate	6×10^{-4}	m ³ /s

Folding under external load. The helix is displacement-loaded and heated for 5 min. in a 120 °C oven, as shown in Fig. 3(b). (Step II) Cooling stage. Cool the helix to 20°C. (Step III) Unloading stage. The external load of the helix is removed at 20 °C. The helix bounces back slightly at this stage. (Step IV): Heating recovery stage. Place the helix in a high-temperature oven (120 °C) or DF-101S Heat Collection-constant Temperature Magnetic Stirrer (built-in 120 °C hot oil), as shown in Fig. 3(c). To place the specimen in the oven, hang the helix horizontally on a thin glass tube to eliminate the effect of gravity. Treat the glass tube surface with alcohol in advance to reduce friction.

4. Results and discussion

The analyses of intelligent helical swimmers are given in two parts: material properties and structural designs. To obtain a more comprehensive evaluation of the shape memory capability of SMPs, we simulate the instantaneous recovery process of SMPs. Section 4.1 presents in detail the numerical results and comparisons with experiments and theory. Subsequently, based on the helical propulsion model proposed in Section 2.2, we use the validated and effective simulation method to calculate the motion indicators of novel nested and uncoiled structures and conduct a comprehensive evaluation of the swimming capabilities. This leads to a design strategy for bio-inspired helical robots.

4.1. Characterization of the thermomechanical properties of SMP-based helix

Fig. 4 shows the deformed process by numerical calculation of the folding and unfolding corresponding to the previous experimental steps. The numerical analysis model of the SMP helix structure uses the finite-element method implemented in ABAQUS®. Notably, after the heating-cooling and loading-unloading cycles, residual stress remains in the helix in the vicinity of the loading end and the fixed end. Fig. 5(a) and (b) compare the results of the finite-element method in Step IV with the gradually deployable morphology of the helix captured experimentally, which verifies the reliability of the numerical results. Furthermore, the smart structure not only regulates the tail length but also regulates the coiling and uncoiling by sensing the environment temperature. The

numerical calculation and experiment are carried out to obtain the thermally induced shape-memory effect of the uncoiling of the helix structure Fig. 5(c) and (d). Here, the fabrication process uses pure resin in the same proportion according to the methods mentioned above. This is attributed to the particularity of the helix structure, whereby the thin aramid filament cannot contain sufficient SMP mixture. The shape change of SMPs is an entropy-driven recovery of a mechanical deformation that occurs through the external stress and is temporarily fixed by the formation of physical crosslinks. Therefore, the stress fixed by SMPs in the filament is too small to overcome the structure's own elasticity and uncoil the helix. The numerical results are consistent with the experimental uncoiled states. The introduction of SMPs into the intelligent helical tail to achieve reconfigurable performance, therefore, could constitute an important step forward in smart-robot applications.

In addition, Fig. 6 shows in detail the mechanical properties resulting from the unique thermal-responsive properties of SMPs. When the temperature is lower than the glass-transition temperature $T_g = 78^\circ\text{C}$, the stress at each point remains steady at a high level. When the temperature reaches the range of T_g to $T_g + 15^\circ\text{C}$, the stress is rapidly released and approaches zero (residual stress remains), as illustrated in Fig. 6(a). Furthermore, Fig. 6(b) shows the relationship between strain and temperature in the four stages of the whole cycle. Our simulation results are basically in agreement with the prediction of standard linear viscoelastic theory, as mentioned above. Notably, during the heating stage (Step IV) under no-load conditions, the strain is significantly recovered in the vicinity of $T_g + 15^\circ\text{C}$. The calculated results for strain recovery express the overall inclination. Given the elastic energy stored in the helix structure, the strain decreases and then increases in Step III, which differs from the horizontal strain recovery curve of the commonly discussed SMP sheet in this step. A small residual strain remains after the cycle, regardless of the theoretical solution and simulation results. Fig. 6(c) demonstrates the displacement in the direction of the length change with respect to time. In contrast with the experimental results, Step III (2 to 3 s) is set in no-load conditions at low temperature in the numerical calculation, but a slight rebound occurs in the experiment. The unfolding process in the numerical calculation occurs instantaneously when the temperature reaches the threshold, which corresponds to the results observed in the experiment. The general rule of length variation predicted by numerical results is consistent with the experiment.

To explore the capacity to recover and to demonstrate a potential application of the intelligent swimmer, the fundamental mechanical performance of the SMP should be tested. In a dynamic mechanical analysis (see Fig. 6(d)), the peak value of the loss of angular tangent appears at the glass-transition temperature. $\log E$ is approximately linear in T_g/T with a slope in the glass-transition region (as shown in Eq. (2)). The present result and the available experimental results [69] both indicate that the modulus varies markedly in the glass-transition region but remains essentially stable above and below the glass-transition region ($T = T_g \pm 15^\circ\text{C}$), which is consistent with theory.

The shape-recovery ratio R_r is the most important indicator to evaluate SMP properties and is expressed as

$$R_r = \frac{s_r - s_b}{s_0} \times 100\%, \quad (8)$$

where s_r is the length of the helix after unfolding, s_b is the rebound displacement after unfolding, and s_0 is the initial length. Given that the external loading is removed after cooling, the elastic energy stored in the helix is released and makes the structure rebound. Therefore, the rebound displacement after unfolding should be considered when calculating. In the experiment, $R_r = 98.4\%$ for the shape memory helix. Note also that, during the folding-unfolding process, in addition to the elongation, the diameter increases by 18.8%.

4.2. Nested and uncoiled design of the helical tail and evaluation of motion

Our previous work [49] shows that the configurations of the single helical tail significantly affect the propulsive motility of the helical swimmer. In consideration of the shape-actuation mechanism, we design the robot structures to further improve the capacity for movement. Two modes of the swimmers with extraordinary structures, the nested helical structures, and uncoiled structures, are established in two separated hydrodynamic cylindrical domains by using COMSOL Multiphysics® (See Appendix for simulation details). The Reynolds number in all subsequent simulation cases is 0.814 (less than 1), so swimming occurs under laminar flow. In the experiment, the overall length of the SMP filament (the tail of the swimming robot) remains constant, and the temperature change triggers the elongation-folding or coiling-uncoiling process. Therefore, the number of turns in these simulation cases is set to 3 and 1.5 for elongation-folding and coiling-uncoiling, respectively, and the pitch increases during unfolding.

The surface average velocity, maximum velocity, and standard deviation of the velocity of the following structures are presented in detail in Fig. 7(a), which shows the head + uniform tail (HUT) structure, the head + hierarchical tail (HHT) structure, the head + uniform tail + hierarchical tail (HUH) structure, the head + uncoiled tail (UCT) structure, the head + stretchy uniform tail + hierarchical tail (HSUH) structure, and the head + stretchy uniform tail + hierarchical tail structure with an overall increased radius (HSUH-R). The surface average velocity and maximum velocity are obtained from the “surface average” and “surface maximum” options in the COMSOL post-processing, respectively, and the standard deviation of velocity is calculated by using the STDEV syntax. A constant acceleration is the desired outcome.

Furthermore, the normalized velocity of the swimming robots is reported to provide a more accurate comparison of performance [72] in Fig. 7(b). Here, we express motility as $U/fL \times 1000$ [19], where U is the linear velocity, f is the rotating frequency, and L is the body length of the swimmer. Notably, the structures with hierarchical tails reveal an impressive advantage in the motility improvement. Compared with the basic HUT structure, the motility of the nested combination of the inner and outer tails (HUH) increases by 54.6%. Meanwhile, the HUH structure makes up for the HHT structure velocity dispersion with a slight increase in maximum velocity. Therefore, nesting is the optimal choice to steadily improve swimming propulsion. In contrast, the velocity of the uncoiled UCT structure decreases compared with that of the HUT structure. When one layer of the nested tails elongates due to thermal driving (i.e., the HSUH structure), no significant change occurs in the average surface velocity or maximum velocity compared with the HUH structure. However, the motility decreases noticeably due to the elongation of the structure. Note also that HSUH-R structure is advantageous regardless of surface average velocity, maximum velocity, and motility for all the types of configurations. Compared with the HSUH structure, the average velocity increases by 116.1% upon increasing the transverse radius. Moreover, compared with the HSUH structure, the HSUH-R structure offers irreplaceable advantages in motility, as shown in Fig. 7(b). Therefore, HSUH-R structure is the best choice for fast-moving applications (e.g., the microswimmers used for cargo delivery, which accelerate the swimming bot and increase the velocity by 226.3%). The Ashby map given in Fig. 7(b) partitions the diverse structures into three levels and objectively evaluates the motion performances, which would have wide-ranging benefits, such as in the biomedical and environmental fields.

Furthermore, we systematically explore the potential advantage of this morphological diversity by building nested or coiled-uncoiled helical swimmers with different body configurations Fig. 8(a)–(f). The forward velocity field around the swimmers, the velocity vectors, maximum and minimum velocity and so on are reported in Fig. 8 to provide a more intuitive comparison of performance. For the structures

with hierarchical tails (e.g., for the HHT structure), the maximum velocity generally occurs in a largest radial pitch area. This is because the trumpet-shaped hierarchical structure concentrates larger thrust force and torque at the far end to drive motion, allowing rotation to dominate the swimming. The radius plays a more important role than the body length in improving speed through geometric structure design.

5. Conclusions

In summary, this paper introduces a type of smart helical swimmer with a nested or uncoiled design that combines the mechanical attributes of remarkable motility with functional characteristics that depend strongly on temperature. Based on the modified linear constitutive model and the symmetric propulsion matrix for the helical propeller, the combined study uses SMP recovery tests, dynamic mechanical tests, a thermomechanical coupling analysis, structural designs, and a hydrodynamics analysis to systematically explore the proposed helical swimmer. In addition, the corresponding comparisons and evaluations are presented and provide guidelines for the manufacture and application of functional swimming microrobots. The results of the study lead to the following main conclusions:

- (1) SMP-based materials can be used to implement temperature-sensitive helical tails of smart swimming robots. The operation is divided into four steps to obtain the shape-memory effect. Given the elastic energy stored in the helix structure, the strain unexpectedly decreases and then increases in the unloading step. As shown by the experimental and simulation results, the shape-recovery process occurs within around 1 to 2 s, with a satisfying shape-recovery ratio of 98.4%.
- (2) The geometrical configurations significantly affect the velocity and motility of swimmers. Based on a hydrodynamics analysis, helix-based robots with nested or uncoiled structural designs are established in two separate cylindrical domains (longitudinal motion and rotation). Notably, the robots with hierarchical tails reveal an impressive advantage in motility because the trumpet-shaped hierarchical structure concentrates larger thrust force and torque at the far end to drive motion, allowing rotation to dominate the swimming.
- (3) A significant increase of 226.3% with respect to existing typical helical swimmers demonstrates that the HSUH-R structure is the optimal choice for applications requiring fast motion. The nested helical structure strategy offers more propulsion than the typical structure. The radius strongly affects the motion performance in robotic systems where rotation is the main actuation. An Ashby map partitions the structures involved in this work into three levels. Finally, an objective evaluation is generated by the structural change of the movement from the perspective of motility and the surrounding flow-field stability feedback.

CRediT authorship contribution statement

Z.Y. Zhang: Conceptualization, Methodology, Writing – original draft, Writing – review & editing. **Y.B. Song:** Writing – review & editing, Methodology. **Y.F. Wang:** Writing – original draft, Writing – review & editing. **C.G. Wang:** Writing – review & editing, Supervision, Funding acquisition, Project administration.

Declaration of Competing Interest

There are no conflicts to declare.

Data availability

No data was used for the research described in the article.

Acknowledgement

This work is supported by National Natural Science Foundation of China 12172102. The authors gratefully thank Mr. W. Zhang and Mrs. X. M. Tang for their thoughtful kindness. The authors would like to express their thanks to the editor and anonymous reviewers whose constructive comments significantly improve the work.

Appendix: Details of numerical modeling

Fig. A1 shows a schematic of the model with the head + uniform tail (HUT) structure as an example. Based on the helical propulsion model proposed in the main text, a low-Re regime implies that the contributions of linear velocity and rotational velocity are additive. Consequently, the numerical modeling can be divided into two independent domains: an external domain to emulate longitudinal motion, and an inner domain to emulate rotation. This distinction significantly simplifies the complexity of the helix motion. The HUT structure is established inside the inner rotating domain (Table A1).

Concerning the geometry of the helical structure (see Fig. A1(a)), (1) we build up the head (a cylinder) and the tail (a helix) in the appropriate spatial positions and use the union selection to combine these two parts. (2) The difference selection is used to distinguish the helical swimmer from the fluid environment. (3) For the mesh, due to the combination of the head and helical tail, the corner needs to be refined. (4) Finally, we choose “form union” to unify the geometry. For the materials setting, the lumen is filled with silicon oil to ensure low Reynolds number. The material parameters are set as Table A1. A laminar flow is implemented by using the computational fluid dynamics module for each part, as shown in Fig. A1(b). Thus, we can emulate a Stokes flow in which inertial terms are rejected. In addition, the no-slip condition is attached to the surface of the helix and the lumen, which ensures that the fluid will have zero velocity relative to these boundaries. The longitudinal motion of the swimmer is achieved by including an input-output flow into the lumen. Here we use the fully developed flow with a flow rate 6×10^{-4} m³/s. To rotate in the inner domain, we must add the moving mesh on cylindrical domain 2. In this case, a moving mesh with rotating angular velocity Ω is implemented and attached to the inner cylinder. Here we set the angular velocity as 31.416 rad/s (corresponding to 5 Hz in the results shown in the main text). A frozen-rotor approximation is included in the numerical calculation to significantly reduce the execution time. In other words, the helical structure inside does not rotate during the execution, however, rotation and the associated momentum terms are imparted to the flow. Therefore, a pseudo-steady-state condition of the helix rotation dynamics is obtained.

References

- [1] Haraguchi T, Tamanaha M, Suzuki K, Yoshimura K, Imi T, Tominaga M, Sakayama H, Nishiyama T, Murata T, Ito K. Discovery of ultrafast myosin, its amino acid sequence, and structural features. Proc Natl Acad Sci USA 2022;119:e2120962119.
- [2] Xu T, Guan Y, Liu J, Wu X. Image-based visual servoing of helical microswimmers for planar path following. IEEE Trans Autom Sci Eng 2019;17:325–33.
- [3] Xu S, Liu J, Yang C, Wu X, Xu T. A learning-based stable servo control strategy using broad learning system applied for microrobotic control. IEEE Trans Cybern 2021;1:1–11.
- [4] Luo M, Feng Y, Wang T, Guan J. Micro-/nanorobots at work in active drug delivery. Adv Funct Mater 2018;28:1706100.
- [5] Dong M, Wang X, Chen XZ, Mushtaq F, Deng S, Zhu C, Torlakci H, Terzopoulou A, Qin XH, Xiao X. 3D-printed soft magnetoelectric microswimmers for delivery and differentiation of neuron-like cells. Adv Funct Mater 2020;30:1910323.
- [6] Li J, de Ávila BEF, Gao W, Zhang L, Wang J. Micro/nanorobots for biomedicine: delivery, surgery, sensing, and detoxification. Sci Robot 2017;2:eaam6431.
- [7] Khalil IS, Adel A, Mahdy H, Micheal MM, Mansour M, Hamdi N, Misra S. Magnetic localization and control of helical robots for clearing superficial blood clots. APL Bioeng 2019;3:026104.
- [8] Zhou H, Mayorga-Martinez CC, Pané S, Zhang L, Pumera M. Magnetically driven micro and nanorobots. Chem Rev 2021;121:4999–5041.

- [9] Zhang Y, Zhang L, Yang L, Vong CI, Chan KF, Wu WK, Kwong TN, Lo NW, Ip M, Wong SH. Real-time tracking of fluorescent magnetic spore-based microrobots for remote detection of *C. diff* toxins. *Sci Adv* 2019;5:eau9650.
- [10] Kim K, Guo J, Liang Z, Fan D. Artificial micro/nanomachines for bioapplications: biochemical delivery and diagnostic sensing. *Adv Funct Mater* 2018;28:1705867.
- [11] Ebbens SJ, Gregory DA. Catalytic Janus colloids: controlling trajectories of chemical microswimmers. *Acc Chem Res* 2018;51:1931–9.
- [12] Aubret A, Youssef M, Sacanna S, Palacci J. Targeted assembly and synchronization of self-spinning microgears. *Nat Phys* 2018;14:1114–8.
- [13] Ahmed D, Baasch T, Jang B, Pane S, Dual J, Nelson BJ. Artificial swimmers propelled by acoustically activated flagella. *Nano Lett* 2016;16:4968–74.
- [14] Garcia-Gradiella V, Sattayasamitsathit S, Soto F, Kuralay F, Yardimci C, Wiitala D, Galarnyk M, Wang J. Ultrasound-propelled nanoporous gold wire for efficient drug loading and release. *Small* 2014;10:4154–9.
- [15] Li K, Chen Z, Xu P. Light-propelled self-sustained swimming of a liquid crystal elastomer torus at low Reynolds number. *Int J Mech Sci* 2022;219:107128.
- [16] Villa K, Novotný F, Zelenka J, Browne MP, Rumil TS, Pumera M. Visible-light-driven single-component BiVO₄ micromotors with the autonomous ability for capturing microorganisms. *ACS Nano* 2019;13:8135–45.
- [17] Chen C, Mou F, Xu L, Wang S, Guan J, Feng Z, Wang Q, Kong L, Li W, Wang J. Light-steered isotropic semiconductor micromotors. *Adv Mater* 2017;29:1603374.
- [18] Nguyen KT, Lee HS, Kim J, Choi E, Park JO, Kim CS. A composite electro-permanent magnetic actuator for microrobot manipulation. *Int J Mech Sci* 2022; 229:107516.
- [19] Huang HW, Uslu FE, Katsamba P, Lauga E, Sakar MS, Nelson BJ. Adaptive locomotion of artificial microswimmers. *Sci Adv* 2019;5:eau1532.
- [20] Huang HW, Sakar MS, Petruska AJ, Pané S, Nelson BJ. Soft micromachines with programmable motility and morphology. *Nat Commun* 2016;7:1–10.
- [21] Abbott JJ, Peyer KE, Lagomarsino MC, Zhang L, Dong L, Kaliakatos IK, Nelson BJ. How should microrobots swim? *Int J Robot Res* 2009;28:1434–47.
- [22] Xu T, Hwang G, Andreff N, Régner S. Influence of geometry on swimming performance of helical swimmers using DoE. *J Micro-Bio Robot* 2016;11:57–66.
- [23] Valdés R, Angeles V, de la Calleja E, Zenit R. Self-propulsion of a helical swimmer in granular matter. *Phys Rev Fluids* 2019;4:084302.
- [24] Miao J, Li X, Liang B, Wang J, Xu X. Enhancing swimming performance by optimizing structure of helical swimmers. *Sensors* 2021;21:494.
- [25] Williams BJ, Anand SV, Rajagopalan J, Saif MTA. A self-propelled biohybrid swimmer at low Reynolds number. *Nat Commun* 2014;5:1–8.
- [26] Sun L, Huang WM, Ding Z, Zhao Y, Wang CC, Purnawali H, Tang C. Stimulus-responsive shape memory materials: a review. *Mater Des* 2012;33:577–640.
- [27] Baniasadi M, Yarali E, Bodaghi M, Zolfagharian A, Baghani M. Constitutive modeling of multi-stimuli-responsive shape memory polymers with multifunctional capabilities. *Int J Mech Sci* 2021;192:106082.
- [28] Baniasadi M, Foyouzat A, Baghani M. Multiple shape memory effect for smart helical springs with variable stiffness over time and temperature. *Int J Mech Sci* 2020;182:105742.
- [29] Liu Y, Du H, Liu L, Leng J. Shape memory polymers and their composites in aerospace applications: a review. *Smart Mater Struct* 2014;23:023001.
- [30] Gao H, Li J, Zhang F, Liu Y, Leng J. The research status and challenges of shape memory polymer-based flexible electronics. *Mater Horiz* 2019;6:931–44.
- [31] Hardy JG, Palma M, Wind SJ, Biggs MJ. Responsive biomaterials: advances in materials based on shape-memory polymers. *Adv Mater* 2016;28:5717–24.
- [32] Johnson AP, Sabu C, Nivitha K, Sankar R, Shirin VA, Henna T, Raphey V, Gangadharappa H, Kotta S, Pramod K. Bioinspired and biomimetic micro-and nanostructures in biomedicine. *J Control Release* 2022;343:724–54.
- [33] Barbot A, Decanini D, Hwang G. Local flow sensing on helical microrobots for semi-automatic motion adaptation. *Int J Robot Res* 2020;39:476–89.
- [34] Liu J, Xu T, Yang SX, Wu X. Navigation and visual feedback control for magnetically driven helical miniature swimmers. *IEEE Trans Ind Inform* 2019;16: 477–87.
- [35] Li J, Li X, Luo T, Wang R, Liu C, Chen S, Li D, Yue J, Cheng SH, Sun D. Development of a magnetic microrobot for carrying and delivering targeted cells. *Sci Robot* 2018;3:eaat8829.
- [36] Chen XZ, Hoop M, Mushtaq F, Siringil E, Hu C, Nelson BJ, Pané S. Recent developments in magnetically driven micro-and nanorobots. *Appl Mater Today* 2017;9:37–48.
- [37] Li H, Tan J, Zhang M. Dynamics modeling and analysis of a swimming microrobot for controlled drug delivery. *IEEE Trans Autom Sci Eng* 2008;6:220–7.
- [38] Gonzalez-Gutierrez J, Osorio-Ramirez S, Solorio-Ordaz FJ, Zenit R. Dynamics of a helical swimmer crossing an interface between two immiscible fluids. *Phys Rev Fluids* 2019;4:083102.
- [39] Ye C, Liu J, Wu X, Wang B, Zhang L, Zheng Y, Xu T. Hydrophobicity influence on swimming performance of magnetically driven miniature helical swimmers. *Micromachines* 2019;10:175.
- [40] Caldag HO, Yesilyurt S. Trajectories of magnetically-actuated helical swimmers in cylindrical channels at low Reynolds numbers. *J Fluids Struct* 2019;90:164–76.
- [41] Irlan YG, Cunha FR. Experimental and theoretical studies of the fluid elasticity on the motion of macroscopic models of active helical swimmers. *Phys Fluids* 2022; 34:053103.
- [42] Xiao W, Du X, Chen W, Yang G, Hu D, Han X. Cooperative collapse of helical structure enables the actuation of twisting pneumatic artificial muscle. *Int J Mech Sci* 2021;201:106483.
- [43] Xu T, Hwang G, Andreff N, Régner S. Planar path following of 3-D steering scaled-up helical microswimmers. *IEEE Trans Robot* 2015;31:117–27.
- [44] Rodenborn B, Chen CH, Swinney HL, Liu B, Zhang H. Propulsion of microorganisms by a helical flagellum. *Proc Natl Acad Sci USA* 2013;110:E338–47.
- [45] Wang X, Hu C, Pané S, Nelson BJ. Dynamic modeling of magnetic helical microrobots. *IEEE Robot Autom Lett* 2021;7:1682–8.
- [46] Xu T, Yu J, Vong CJ, Wang B, Wu X, Zhang L. Dynamic morphology and swimming properties of rotating miniature swimmers with soft tails. *IEEE-ASME Trans Mechatron* 2019;24:924–34.
- [47] Palagi S, Fischer P. Bioinspired microrobots. *Nat Rev Mater* 2018;3:113–24.
- [48] Kaneh P, Ishikawa T. Fluid mechanics of swimming bacteria with multiple flagella. *Phys Rev E* 2014;89:042704.
- [49] Zhang Z, Wang Y, Kang J, Qiu X, Wang C. Helical micro-swimmer: hierarchical tail design and propulsive motility. *Soft Matter* 2022;18:6148–56.
- [50] Lendlein A, Langer R. Biodegradable, elastic shape-memory polymers for potential biomedical applications. *Science* 2002;296:1673–6.
- [51] Mohr R, Kratz K, Weigel T, Lucka-Gabor M, Moneke M, Lendlein A. Initiation of shape-memory effect by inductive heating of magnetic nanoparticles in thermoplastic polymers. *Proc Natl Acad Sci USA* 2006;103:3540–5.
- [52] Yan X, Wang F, Zheng B, Huang F. Stimuli-responsive supramolecular polymeric materials. *Chem Soc Rev* 2012;41:6042–65.
- [53] Palagi S, Mark AG, Reigh SY, Melde K, Qiu T, Zeng H, Parmeggiani C, Martella D, Sanchez-Castillo A, Kapernaum N. Structured light enables biomimetic swimming and versatile locomotion of photoresponsive soft microrobots. *Nat Mater* 2016;15: 647–53.
- [54] Purcell EM. The efficiency of propulsion by a rotating flagellum. *Proc Natl Acad Sci USA* 1997;94:11307–11.
- [55] Dong R, Cai Y, Yang Y, Gao W, Ren B. Photocatalytic micro/nanomotors: from construction to applications. *Acc Chem Res* 2018;51:1940–7.
- [56] Behkam B, Sitti M. Design methodology for biomimetic propulsion of miniature swimming robots. *J Dyn Syst Trans ASME* 2006;128:36–43.
- [57] Kosa G, Jakab P, Jolesz FA, Hata N. Swimming capsule endoscope using static and RF magnetic field of MRI for propulsion. In: Proceedings of the IEEE international conference on robotics and automation; 2008. p. 2922–7.
- [58] Kosa G, Shoham M, Zaaroor M. Propulsion method for swimming microrobots. *IEEE Trans Robot* 2007;23:137–50.
- [59] Yesin KB, Vollmers K, Nelson BJ. Modeling and control of untethered biomicrorobots in a fluidic environment using electromagnetic fields. *Int J Robot Res* 2006;25:527–36.
- [60] Zhang L, Abbott JJ, Dong L, Kratochvil BE, Bell D, Nelson BJ. Artificial bacterial flagella: fabrication and magnetic control. *Appl Phys Lett* 2009;94:064107.
- [61] Mathieu JB, Beaudoin G, Martel S. Method of propulsion of a ferromagnetic core in the cardiovascular system through magnetic gradients generated by an MRI system. *IEEE Trans Biomed Eng* 2006;53:292–9.
- [62] Huang HW, Chao Q, Sakar MS, Nelson BJ. Optimization of tail geometry for the propulsion of soft microrobots. *IEEE Robot Autom Lett* 2017;2:727–32.
- [63] Angeles V, Godínez FA, Puente-Velázquez JA, Méndez-Rojano R, Lauga E, Zenit R. Front-back asymmetry controls the impact of viscoelasticity on helical swimming. *Phys Rev Fluids* 2021;6:043102.
- [64] Quispe JE, Oulmas A, Régner S. Geometry optimization of helical swimming at low Reynolds number. In: Proceedings of the IEEE international conference on manipulation, automation and robotics at small scales; 2019. p. 1–6.
- [65] Zhao F, Rong W, Wang L, Sun L. Magnetic actuated shape-memory helical microswimmers with programmable recovery behaviors. *J Bionic Eng* 2021;18: 799–811.
- [66] Yoshida K, Onoe H. Soft spiral-shaped microswimmers for autonomous swimming control by detecting surrounding environments. *Adv Intell Syst* 2020;2:2000095.
- [67] Yarali E, Taheri A, Baghani M. A comprehensive review on thermomechanical constitutive models for shape memory polymers. *J Intell Mater Syst Struct* 2020;31: 1243–83.
- [68] Tobushi H, Hashimoto T, Hayashi S, Yamada E. Thermomechanical constitutive modeling in shape memory polymer of polyurethane series. *J Intell Mater Syst Struct* 1997;8:711–8.
- [69] Tobushi H, Okumura K, Hayashi S, Ito N. Thermomechanical constitutive model of shape memory polymer. *Mech Mater* 2001;33:545–54.
- [70] Xue Y, Lei J, Liu Z. A thermodynamic constitutive model for shape memory polymers based on phase transition. *Polymer* 2022;243:124623.
- [71] Gray J, Hancock G. The propulsion of sea-urchin spermatozoa. *J Exp Biol* 1955;32: 802–14.
- [72] Dreyfus R, Baudry J, Roper ML, Fermigier M, Stone HA, Bibette J. Microscopic artificial swimmers. *Nature* 2005;437:862–5.